

ISSN 2052-5206

Received 28 October 2021 Accepted 17 March 2022

Edited by T. B. Bekker, Siberian Branch of Russian Academy of Science, Russian Federation

Keywords: crystal growth; garnet crystals; micro-pulling-down; multicomponent oxide.

Supporting information: this article has supporting information at journals.iucr.org/b

Effects of composition and growth parameters on phase formation in multicomponent aluminum garnet crystals

Matheus Pianassola, a,b* Marlena Alexander, a,b Bryan Chakoumakos, C Merry Koschan, Charles Melcher a,b,d and Mariya Zhuravleva a,b

^aScintillation Materials Research Center, University of Tennessee, Knoxville, TN 37996, USA, ^bDepartment of Materials Science and Engineering, University of Tennessee, Knoxville, TN 37996, USA, ^cNeutron Scattering Division, Oak Ridge National Laboratory, Oak Ridge, TN 37831, USA, and ^dDepartment of Nuclear Engineering, University of Tennessee, Knoxville, TN 37996, USA. *Correspondence e-mail: mpianass@vols.utk.edu

The effects of composition on the phase formation of multicomponent garnet crystals grown via directional solidification by the micro-pulling-down method are studied. A relatively wide range of rare-earth (RE) average ionic radii (AIR) is explored by formulating ten compositions from the system (Lu,Y,Ho,Dy,Tb,Gd)₃Al₅O₁₂. Crystals were grown at either 0.05 or 0.20 mm min⁻¹. The hypothesis is that multicomponent compounds with large AIR will form secondary phases as the single-RE aluminum garnets formed by larger Tb³⁺ or Gd³⁺; this will result in crystals of poor optical quality. Crystals with large AIR have a central opaque region in optical microscopy images, which is responsible for their reduced transparency compared to crystals with small AIR. Slow pulling rates suppress the formation of the opaque region in crystals with intermediate AIR. Powder and single-crystal X-ray diffraction and electron probe microanalysis results indicate that the opaque region is a perovskite phase. Scanning electron microscopy and energy dispersive spectroscopy measurements reveal eutectic inclusions at the outer surface of the crystals. The concentration of the eutectic inclusions increases with increasing AIR.

1. Introduction

A surprising phase stabilization and attractive functional properties have been reported for oxides containing five cations that fractionally occupy the same crystallographic site (Rost et al., 2015; Musicó et al., 2020). Such complex compositions are usually called 'high-entropy' or 'multicomponent' (Dienadic et al., 2017; Pianassola, Loveday, McMurray et al., 2020; Karati et al., 2021; Sun et al., 2020). Admixing two or three elements in garnet crystals has been shown to improve scintillation properties (Kamada et al., 2011, 2014; Prusa et al., 2013; Chewpraditkul et al., 2018). Therefore, multicomponent crystals could lead to further improvement in performance for radiation detection in medical imaging and homeland security applications. To date, only two multicomponent aluminum garnet compounds have been reported with five or more rare-earth (RE) elements, one synthesized as a polycrystalline ceramic (Chen et al., 2020) and one as a single crystal (Pianassola, Loveday, Chakoumakos et al., 2020). Further study on composition design and crystal growth of garnets containing multiple REs is needed to establish a correlation between composition and phase formation, and to guide future investigation into fundamental and functional properties in single crystals.

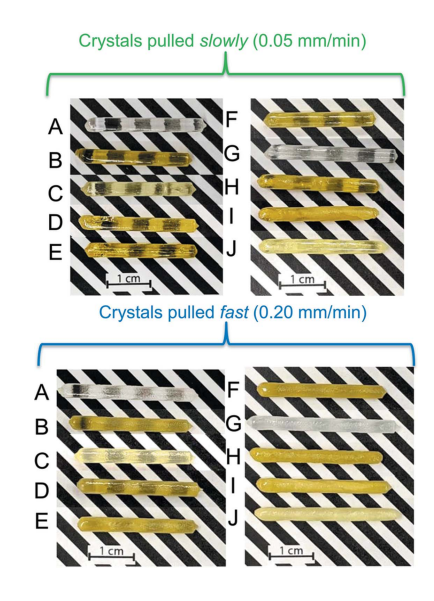


Table 1
List of compositions with respective stoichiometric coefficients for each RE element and Y, and resulting AIR of REs in order of increasing AIR (Shannon & Prewitt, 1969).

	Fraction of REs and Y in (Lu,Y,Ho,Dy,Tb,Gd) ₃ Al ₅ O ₁₂									
Composition ID	Lu	Y	Но	Dy	Tb	Gd	AIR of REs and Y (Å)	RE with closest ionic radius	Type of precursor powder	
A	$\frac{1}{4}$	$\frac{1}{4}$	_	_	$\frac{1}{4}$	<u>1</u> 4	1.021	Ho ³⁺	R	
В	4 1 4	-	$\frac{1}{4}$	_	1/4	1 4	1.023	Ho ³⁺	R	
C	1/4	_	_	$\frac{1}{4}$	1/4	1/4	1.025	Ho ³⁺	R	
D	1/6	$\frac{1}{6}$	1/6	_	1/4	1/4	1.026	Dy^{3+}	R	
E	1/6	_	1/6	$\frac{1}{6}$	1/4	1/4	1.028	Dy^{3+}	R	
F	1/8	_	1/4	1/8	1/4	1/4	1.030	Dy ³⁺	R	
G	_	$\frac{1}{2}$	_	_	1/4	1/4	1.033	Dy^{3+}	R	
H	_	_	$\frac{1}{2}$	_	1/4	1 4	1.035	Dy ³⁺	R and P	
I	_	_	1/4	$\frac{1}{4}$	1/4	1 4	1.038	Tb ³⁺	R and P	
J	_	_	_	1/2	1/4	1/4	1.040	Tb^{3+}	R and P	

Notes: '-' denotes element not included in the composition, 'R' is raw precursor powder (mixture of sesquioxides) and 'P' is pre-synthesized precursor powder (multicomponent aluminium garnet).

The phase stabilization of multicomponent oxides has been attributed to an entropy-driven mechanism (Rost et al., 2015), but the composition and synthesis method can also affect phase formation in polycrystalline samples (Djenadic et al., 2017; Pianassola, Loveday, McMurray et al., 2020). In the case of crystals grown via directional solidification, the formation of a single phase also depends on melt congruency and elemental segregation. While there are several publications on multicomponent oxide thin films (Meisenheimer et al., 2017; Kotsonis et al., 2020, 2018; Sivakumar et al., 2018; Liang et al., 2021; Jacobson et al., 2021; Patel et al., 2020; Nguyen et al., 2020; Braun et al., 2018; Sharma et al., 2018, 2021; Chen et al., 2021; Kirnbauer et al., 2019), only a few reports demonstrate the growth and phase formation in multicomponent oxide bulk crystals (Pianassola, Loveday, Chakoumakos et al., 2020; Pianassola et al., 2021; Greculeasa et al., 2020; Liu et al., 2021; Kinsler-Fedon et al., 2020). We previously demonstrated the growth of a six-component aluminum garnet (Lu_{1/6}Y_{1/6}Ho_{1/6}- $Dy_{1/6}Tb_{1/6}Gd_{1/6})_3Al_5O_{12}$ that melted congruently, formed a single phase, and was grown with excellent optical quality and reproducibility (Pianassola, Loveday, Chakoumakos et al., 2020). That work focused on only one composition with RE elements in equiatomic amounts; here Y is referred to as an RE element for simplicity. The effect of non-equiatomic compositions on phase formation in multicomponent garnets remains unexplored.

The correlation between RE³⁺ ionic radius and fundamental properties of one-RE aluminum garnets suggests that the Average Ionic Radius (AIR) of REs in multicomponent crystals may affect phase formation. In the garnet structure, RE³⁺ occupy dodecahedral crystallographic sites and have coordination number (CN) VIII, while Al³⁺ ions occupy tetrahedral and octahedral sites with CN IV and VI, respectively. Due to the small size of the dodecahedral site, only Gd³⁺ and REs smaller than Gd³⁺ form thermodynamically stable single-RE garnets (Wu & Pelton, 1992). For the same

reason, smaller REs are preferentially incorporated in multicomponent crystals grown from the melt (Pianassola, Loveday, Chakoumakos *et al.*, 2020). Smaller REs also form congruently melting garnets, while larger Tb³⁺ and Gd³⁺ form garnets that melt incongruently. Additionally, as the RE³⁺ ionic radius increases, the composition of the eutectic formed between single-RE RE₃Al₅O₁₂ (garnet stoichiometry) and Al₂O₃ is closer to the garnet stoichiometry (Wu & Pelton, 1992; Bondar *et al.*, 1984).

In this work, we determine the effects of composition and AIR on the formation of a single phase in garnet crystals grown by pulling from the melt. In single-RE aluminum garnets there is a transition from congruent to incongruent melting between Dy₃Al₅O₁₂ and Tb₃Al₅O₁₂. Therefore, we expect multicomponent compositions with an AIR equal to or smaller than that of Dy³⁺

(1.030 Å for CN VIII; Shannon & Prewitt, 1969) to melt congruently and solidify into a single garnet phase, while we expect compositions with an AIR approaching that of Tb^{3+} (1.040 Å for CN VIII; Shannon & Prewitt, 1969) to melt incongruently and form detrimental secondary phases during solidification. We expand on our previously explored multicomponent garnet system ($\mathrm{Lu}_{1/6}\mathrm{Y}_{1/6}\mathrm{Ho}_{1/6}\mathrm{Dy}_{1/6}\mathrm{Tb}_{1/6}\mathrm{Gd}_{1/6}$)₃Al₅O₁₂ (AIR = 1.023 Å) and formulate ten nonequiatomic compositions using the same five RE elements and Y, with an AIR in the range 1.021–1.040 Å. Here we design the AIR by varying the relative fractional occupation of the dodecahedral crystallographic site by Lu, Y, Ho, and Dy. The fractions of REs that form incongruent single-RE aluminum garnet (Tb and Gd) are kept constant at 1/4. We also investigate the effect of elemental segregation on phase formation.

We used the micro-pulling-down method (mPD) to grow the crystals. This method is ideally suited for this study due to its ability to produce compositionally homogenous crystals with minimal axial elemental gradient (Fukuda & Chani, 2007). Additional advantages of the mPD method include the use of relatively small amounts of expensive raw materials (~1 g per crystal) and faster pulling rates (0.05–20 mm min⁻¹) compared to scalable growth methods, such as the Czochralski technique.

2. Experimental

2.1. Compositions

Our approach to study the effects of AIR of REs on phase formation of garnet crystals involves formulating multicomponent compounds with various AIR. We designed ten compositions within the (Lu,Y,Ho,Dy,Tb,Gd)₃Al₅O₁₂ system by varying the relative atomic fractional occupation of the dodecahedral crystallographic site by Lu, Y, Ho, and Dy. The fractions of Tb and Gd, which form incongruent melting

single-RE aluminum garnets, were held constant at $\frac{1}{4}$ each; therefore, 50 at% of the REs in all compositions form incongruent single-RE aluminum garnets. The ionic radii of Lu³⁺, Y³⁺, Ho³⁺, Dy³⁺, Tb³⁺, and Gd³⁺ for coordination number VIII are 0.970, 1.015, 1.020, 1.030, 1.040, and 1.060 Å, respectively (Shannon & Prewitt, 1969). A list of compositions with the stoichiometric coefficient of each RE element and Y and the respective AIR of REs is shown in Table 1 in order of increasing the AIR.

2.2. Starting materials

To study the effect of the type of precursor powder on phase formation, we used two types of precursor powders, namely, raw and pre-synthesized. Raw powders were mixtures of raw oxides, while pre-synthesized powders were single-phase multicomponent garnet powders.

2.2.1. Raw precursor powder. To prepare raw precursor powders, the following powder oxides of at least 99.99% purity were dried at 800 °C for 8 h in air and mixed in stoichiometric ratios: Lu₂O₃, Y₂O₃, Ho₂O₃, Dy₂O₃, Tb₂O₃, Gd₂O₃ and Al₂O₃.

2.2.2. Pre-synthesized precursor powder. Pre-synthesized powders were prepared *via* polymeric steric entrapment (Nguyen *et al.*, 1999). Two aqueous solutions were prepared, *i.e.* a cation solution and a polymer solution. In the cation solution, stoichiometric amounts of nitrate salts were dissolved in deionized water. The following nitrates of at least 99.99% purity were used as cation sources: Lu(NO₃)₃·6H₂O, Y(NO₃)₃·6H₂O, Ho(NO₃)₃·5H₂O, Dy(NO₃)₃·5H₂O, Tb-

Y(NO₃)₃·6H₂O, Ho(NO₃)₃·5H₂O, Dy(NO₃)₃·5H₂O, Tb-(NO₃)₃·6H₂O, Gd(NO₃)₃·6H₂O, and Al(NO₃)₃·9H₂O. In the polymer solution, a stoichiometric amount of polyvinyl alcohol (PVA) was dissolved; the PVA had a molecular weight of 9–10 kg mol⁻¹ and was 80% hydrolyzed. The proportion of PVA to the cation source was such that the ratio of positive to negative charges was 4:1; the positive charges come from the valence of the cations and the negative charges come from the hydroxyl functional group (OH) of PVA. The two solutions were continuously agitated at room temperature. After complete dissolution of nitrates and PVA, the solutions were combined and the mixture was continuously agitated and heated to ~85 °C to evaporate the water. The resulting foamtype material was dried overnight in air at 180 °C; the dried foam was then calcined in air at 550 °C for 2 h, followed by crystallization in air at 900 °C for 1 h.

2.3. Crystal growth

Cylindrical crystals of 3 mm diameter were grown by the mPD method using a KDN Dai-Ichi Kiden furnace with an RF generator model TR-02001 operated at 26 kVA. A \oslash 16 mm iridium crucible with a \oslash 3 mm die and a \oslash 0.5 mm capillary channel was used as a melt reservoir. A Czochralski-grown Lu₃Al₅O₁₂ crystal was used as seed to initiate the growth. Two 1 g crystals of each composition listed in Table 1 were grown from raw precursor powders, one at 0.05 mm min⁻¹ (slow pulling rate) and the other at 0.20 mm min⁻¹ (fast pulling rate), to study the effect of pulling rate on crystal quality. One 0.3–0.5 g crystal of compositions H, I, and J was grown from

pre-synthesized powder at $0.05~\rm mm~min^{-1}$ to study the effect of the type of precursor powder on phase formation. A molten-zone height of $\sim\!200~\mu m$ was maintained for all growth experiments by adjusting the power of the RF generator. A previous publication includes details about the mPD method and the crystal growth set-up used (Pianassola, Loveday, Chakoumakos *et al.*, 2020).

2.4. Optical microscopy

To evaluate the optical quality of the crystals, a 1 mm-thick cross sectional sample was cut from each crystal. The samples were cut 2 mm apart from the seed end. After polishing the samples, a Leica MC170 HD microscope camera was used to obtain optical images.

2.5. Scanning electron microscopy and energy dispersive spectroscopy

The samples used for optical microscopy were also imaged using a Zeiss EVO MA15 Scanning Electron Microscope (SEM). The SEM instrument is equipped with a Bruker xFlash 6130 Energy Dispersive X-ray Spectrometer (EDS), which was used to analyze the elemental composition of inclusions.

2.6. Powder X-ray diffraction

Phase identification was conducted by acquiring powder X-ray diffraction (PXRD) patterns of all crystals. Crystals were cut into three cylindrical sections of equal lengths, and the middle section was used for phase analysis. A PANalytical Empyrean diffractometer was used to obtain diffraction patterns. The instrument operates in the Bragg–Brentano geometry using a Cu $K\alpha$ X-ray source at 45 kV and 40 mA. Unit-cell parameter and phase composition were obtained *via* Rietveld refinements with the General Structure Analysis System II software (*GSASII*). A goodness-of-fit value smaller than 1.60 was achieved for all refinements.

2.7. Single-crystal X-ray diffraction

To identify differences in the crystal structure in the center and the surface of the crystals, samples cut from the center and outer surface of selected crystals were analyzed using single-crystal XRD. These samples were cut 2 mm away from the seed end. Two crystals grown from raw precursor powders were selected, *i.e.* crystal C grown at 0.20 mm min⁻¹ and crystal I grown at 0.05 mm min⁻¹. The former was selected from a group of transparent crystals and the latter from a group of crystals that are transparent in the outer surface and have a central opaque region.

A Rigaku XtaLAB PRO diffractometer was used to collect single-crystal diffraction data at 270 K using a Rigaku HyPix-6000HE detector and an Oxford N-HeliX cryocooler and graphite-monochromated Mo $K\alpha$ radiation (λ = 0.71073 Å, 50 kV and 40 mA). The Rigaku Oxford Diffraction CrysAlis PRO software was used for peak indexing and integration (Rigaku OD, 2015). An empirical absorption correction was applied using the SCALE3 ABSPACK algorithm, as implemented in CrysAlis PRO. The SHELXL2013 (Sheldrick,

2015) and *WinGX* (Farrugia, 2012) software packages were used for data processing and structure refinement. The structure refinements were made with O-atom positional coordinates, anisotropic atomic displacement parameters, an extinction parameter, and the scale factor.

2.8. Electron microprobe analysis

The radial elemental distribution in selected crystals was investigated by Electron Probe Micro Analysis (EPMA). Radial sections of 1 mm thickness were cut 2 mm away from the seed end of crystals of compositions A and J. that were grown at 0.05 mm min⁻¹. The samples were embedded in epoxy and a CAMECA SX100 Electron Microprobe was used for elemental composition analysis. The instrument is equipped with high-speed Back-Scattered Electron (BSE) detectors and four Wavelength-Dispersive Spectrometers (WDS). Images were obtained by detecting the back-scattered electrons and compositional information was acquired by detecting characteristic X-rays by WDS. The instrumental voltage and current were 15 kV and 30 nA, respectively. The probe point size was 1 µm and the diameter of the excitation area was in the range 2-3 μm. Radial elemental distribution profiles were obtained by collecting data at 100 µm steps.

3. Results and discussion

3.1. Grown crystals

Higher optical quality was obtained for crystals grown using slower pulling rates and for compositions with smaller AIR. In Fig. 1, crystals of compositions A–J grown from raw powders are grouped according to their respective pulling rate. In general, crystals pulled slowly (0.05 mm min⁻¹) are more transparent than crystals pulled fast (0.20 mm min⁻¹). Additionally, within each group, crystals of compositions with smaller AIR (A–E) are more transparent than those of compositions with larger AIR (F–J). Cracking may contribute to the reduced transparency of the crystals with larger AIR and fast pulling rate. The surface roughness of crystals pulled fast may be related to a more pronounced thermal etching due to the relatively higher temperatures necessary to maintain a stable molten zone for growth at high pulling rates using the mPD method.

Optical microscope images revealed that a central opaque region occurs in crystals with large AIR and grown using fast pulling rates. 1 mm-thick cross sections of crystals grown from raw precursor powders are shown in Fig. 2. For crystals pulled slowly, crystals A–G are transparent, while crystals H–J (larger AIR) have a central opaque region. On the other hand, for crystals pulled fast, crystals A–D are transparent throughout, and crystals E–J (larger AIR) have a central opaque region. This opaque region explains the reduced transparency of crystals with large AIR as seen in Fig. 1. Additionally, all crystals have small dark inclusions close to their outer surface, which are more pronounced for crystals pulled fast. A correlation of the opaque central regions with

phase formation is discussed in §3.2 and §3.3; we also discuss the nature of the small dark inclusions in §3.4.

To investigate whether the nature of the precursor powder affects the formation of the central opaque region, crystals of composition H–J were also grown from raw powders using a slow pulling rate (0.05 mm min⁻¹). These three compositions are the only ones that formed a central opaque region in crystals grown from raw powder and pulled slowly (Fig. 2). As

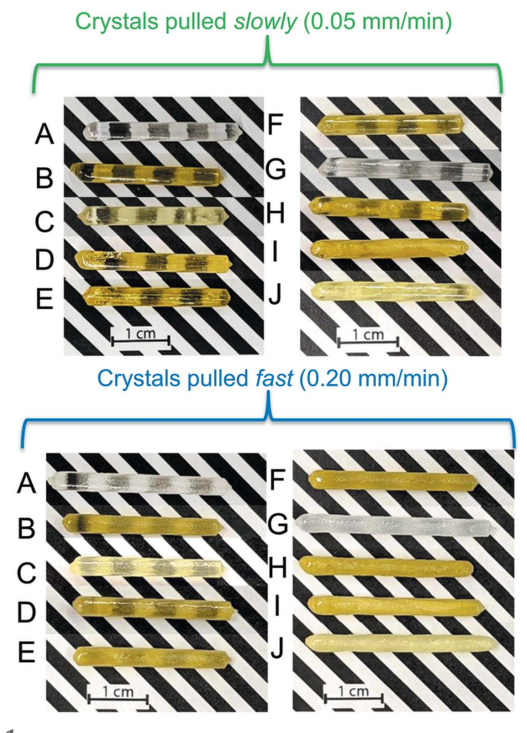


Figure 1
Crystals grown from raw powders; crystal IDs A–J correspond to the compositions listed in Table 1. The yellow color seen in most crystals comes from Ho and/or Dy. Slower pulling rates and compositions with smaller AIR lead to better optical quality.

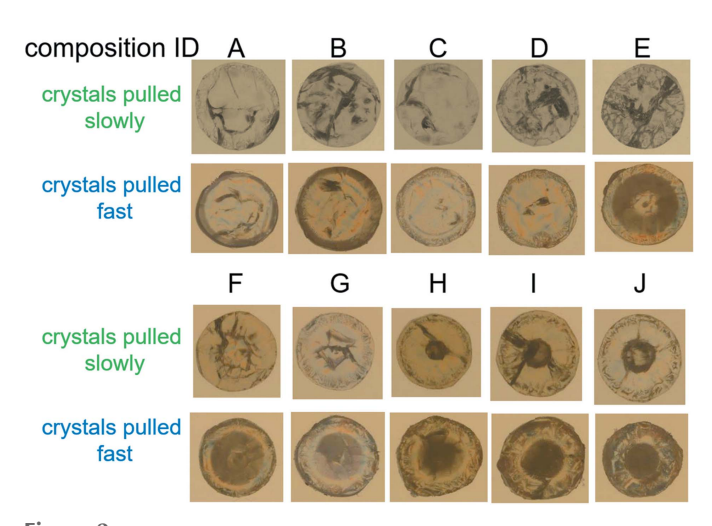


Figure 2 Optical microscope images of 1 mm-thick radial sections cut 2 mm away from the seed end of crystals. Composition ID and pulling rates are indicated in the figure. A central opaque region is present in crystals H–J, which were pulled slowly, and crystals E–J, which were pulled fast.

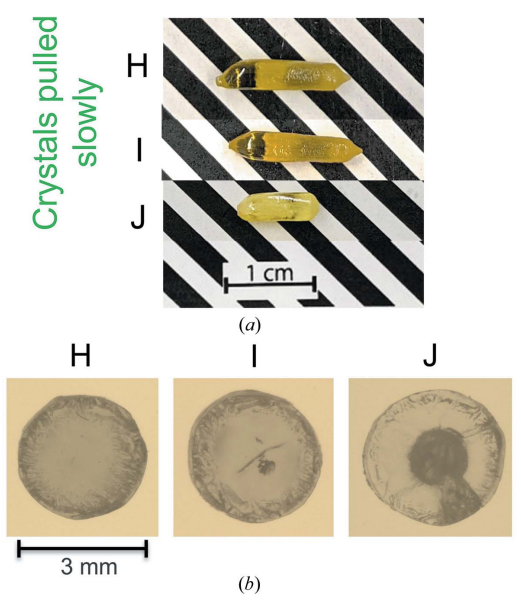


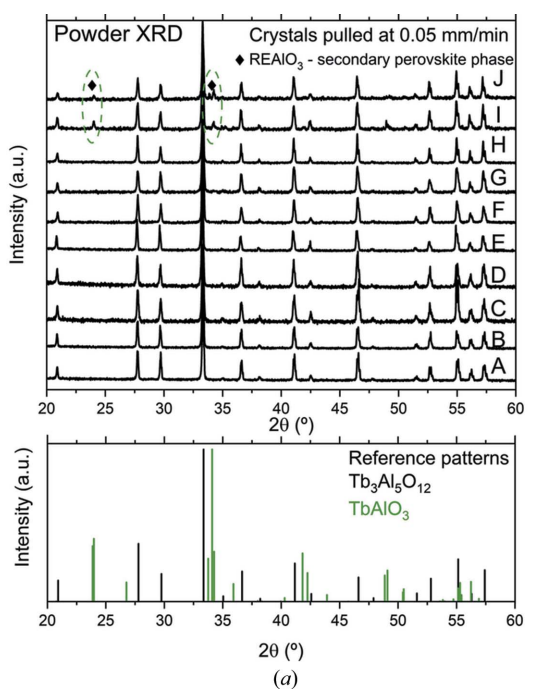
Figure 3(a) Crystals grown from pre-synthesized powders; crystal IDs H–J correspond to the compositions listed in Table 1. (b) Optical microscope images of 1 mm-thick radial sections cut 2 mm away from the seed end of crystals grown from pre-synthesized powders. Composition IDs are indicated in the figure.

shown in Fig. 3(a), the transparency of crystals H and I improved compared to the crystals grown from raw powders and pulled slowly (Fig. 1). However, the transparency of crystals H and I in Fig. 3(a) is still inferior to that of crystals with smaller AIR (A–E) grown from raw powders (Fig. 1). The transparency of crystal J in Fig. 3(a) is similar to that of

crystal J grown from raw powder and pulled slowly (Fig. 1). Optical images of 1 mm sections of the crystals grown from raw materials are shown in Fig. 3(b). Crystals H and I are transparent across the entire diameter, while crystal J has a central opaque region. A comparison of crystals H–J grown from pre-synthesized powders [Fig. 3(b)] with crystals of the same composition grown from raw powders (Fig. 2) indicates that starting with pre-synthesized powders prevents the formation of an opaque phase for compositions H and I, but not for J, which has the largest AIR in this study.

3.2. Phase formation and crystal structure

3.2.1. Powder X-ray diffraction (PXRD). The majority of the crystals grown from raw powders formed the desired single garnet phase, even though the nominal compositions have 50% of the dodecahedral sites occupied by Tb and Gd (25% each), which form incongruent melting Tb₃Al₅O₁₂ and Gd₃Al₅O₁₂ (Wu & Pelton, 1992). The PXRD patterns of crystals grown slowly are shown in Fig. 4(a); reference patterns of Tb₃Al₅O₁₂ (Hammann, 1969) and TbAlO₃ (Bombik et al., 2003) are included for comparison. These patterns indicate a single garnet phase with space group $Ia\overline{3}d$ (Tb₃Al₅O₁₂, ICSD #33602) for compositions A-H (smaller AIR), while compositions I–J (larger AIR) have a secondary perovskite phase with space group Pbnm (TbAlO₃, ICSD #84422). On the other hand, the PXRD patterns of crystals grown fast indicate a single garnet phase for compositions A-E (smaller AIR), while compositions F-J (larger AIR) have a secondary perovskite phase, as seen in Fig. 4(b). Therefore, a single phase can be obtained for melt-grown crystals having relatively large



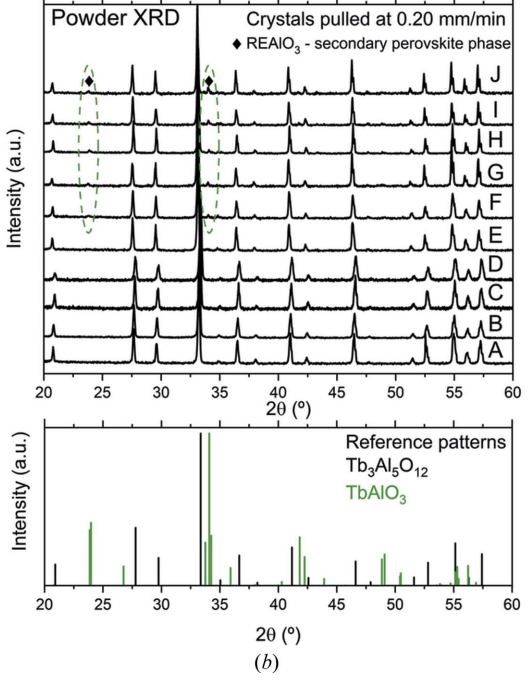


Figure 4
PXRD patterns of crystals grown from raw powders and pulled (a) slowly and (b) fast. Reference patterns for Tb₃Al₅O₁₂ (ICSD #33602) and TbAlO₃ (ICSD #84422) are presented at the bottom for comparison. Crystals A–H pulled slowly and crystals A–E pulled fast have a single garnet phase. Reflection peaks of secondary perovskite phases are indicated by a dashed oval.

Table 2 Phase composition obtained from Rietveld refinement for crystals of compositions A-J pulled slowly $(0.05~\mathrm{mm~min}^{-1})$ and fast $(0.20~\mathrm{mm~min}^{-1})$.

		Phase composition (wt%)									
Crystal composition ID		A	В	С	D	Е	F	G	Н	I	J
Crystals pulled slowly	Garnet Perovskite								100		90 10
Crystals pulled fast		100	100	100	100	100	87 13	88 12	81 19		88 12

amounts of large REs, such as Tb and Gd, but the AIR should be maintained below 1.038 Å, which here corresponds to the composition I (Table 1).

Table 2 is a list of phase compositions obtained from Rietveld refinement for all crystals grown from raw precursor powders. The amount of perovskite phase does not exceed 20 wt% and its presence may be related to the central opaque area seen in crystals with large AIR (Fig. 2), which is discussed using single-crystal XRD data in §3.2.2 and EPMA in §3.3.

As the AIR of multicomponent garnets increases, the tendency to melt incongruently may also increase, as in the case of single-RE RE₃Al₅O₁₂ (Wu & Pelton, 1992). Compounds with large AIR may melt incongruently, which explains the crystallization of a mixture of garnet and perovskite phases. Interestingly, crystals of compositions F–H form a single garnet phase when pulled slowly but have a secondary perovskite phase when pulled fast. This indicates that for those compositions a slow growth rate may favor the incorporation of relatively large REs into the small dodecahedral site of the garnet phase. On the other hand, faster pulling rates lead to the formation of a secondary orthorhombic perovskite structure, which has larger dodecahedral sites that easily accommodate large RE elements (Li & Sakka, 2015).

Crystals H and I grown from pre-synthesized powders formed the desired single garnet phase, while crystal J has a secondary perovskite phase, as seen in the PXRD patterns in Fig. 5. This indicates that using pre-synthesized powders prevents the formation of a perovskite phase in composition I, but not in J, which has the largest AIR in this study. The phase fraction of the primary garnet structure in crystal J is 85 wt%, which was obtained *via* Rietveld refinement. This phase fraction of crystal J grown from pre-synthesized powder is slightly smaller than that of crystal J grown from raw powder (88 wt%; Table 2).

3.2.2. Single-crystal XRD. To compare the structure of the center and surface of the crystals, single-crystal XRD data were collected and analyzed for crystals C and I grown from raw precursor powder at 0.20 and 0.05 mm min⁻¹. The supporting information contains the single-crystal X-ray diffraction refinement parameters in Table S1 and the fractional atomic coordinates and equivalent isotropic displacement parameters in Table S2. Crystal C is a single garnet phase (space group $Ia\overline{3}d$) and the lattice parameter is larger in the outer surface [12.0703 (3) Å] than in the center

[12.0516 (4) Å], as seen in Table S1. This indicates a segregation of larger REs to the outer surface of the crystals, which is discussed in §3.3 and has been observed previously in multicomponent aluminum garnet crystals grown via the mPD method (Pianassola, Loveday, Chakoumakos et al., 2020). The outer surface of crystal I is also a single garnet phase (space group $Ia\overline{3}d$) and has a larger unit-cell parameter [12.0892 (2) Å] than that of crystal C, which is expected since the AIR of composition I is larger than that of composition C (Table 1). The diffraction pattern obtained for the center of crystal I is typical of a perovskite structure, which could not be confidently refined because the particular distortion is uncertain. The quality of the data was poor, possibly due to chemical inhomogeneity, twinning, and the presence of multiple misaligned grains, which would explain the opacity of the central region of the crystal as shown in Fig. 2.

3.3. Radial elemental distribution

To understand how AIR affects radial elemental profiles, EPMA data were collected for crystals A and J pulled slowly. Crystal A has the smallest AIR in this study and is transparent, while crystal J has the largest AIR and has a central opaque region (Table 1 and Fig. 2). A microscope image and the EPMA results of crystal A (Lu_{1/4}Y_{1/4}Tb_{1/4}Gd_{1/4})₃Al₅O₁₂ are shown in Fig. 6(*a*); the RE and Y concentration profiles are continuous and located in the vicinity of the nominal concentration (3.75 at%). Additionally, smaller elements (Lu

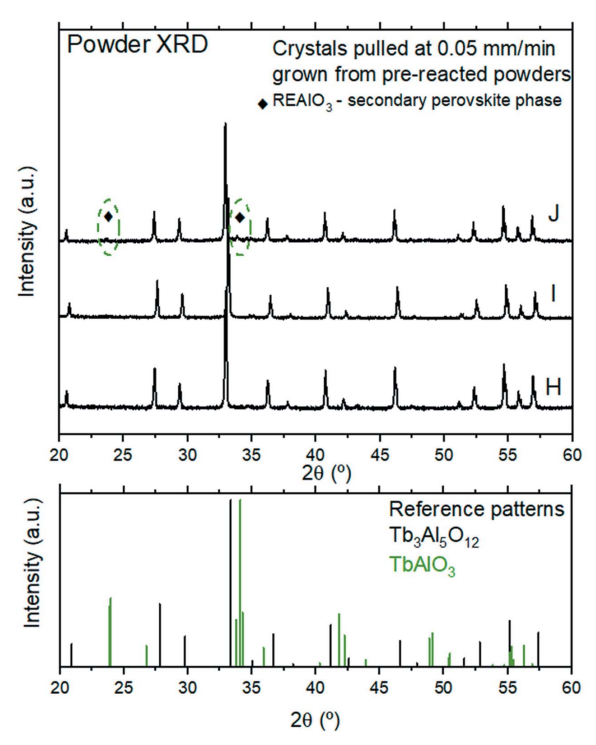


Figure 5
PXRD patterns of crystals H–J grown from pre-synthesized powders and pulled slowly. Reference patterns for Tb₃Al₅O₁₂ (ICSD #33602) and TbAlO₃ (ICSD #84422) are presented at the bottom for comparison. Crystals H–I have a single garnet phase. Reflection peaks of secondary perovskite phases are indicated by a dashed oval.

and Y) have downwardly curved profiles (higher concentrations in the center of the crystal), while larger elements (Tb and Gd) have upwardly curved profiles (higher concentrations in the outer surface of the crystal). This is typical of multicomponent aluminum garnet crystals and indicates the preferential incorporation of smaller REs into the small dodecahedral crystallographic sites of the garnet structure. The rejected larger REs cannot accumulate in the crucible since mPD crystals are grown without direct contact with the melt reservoir. Therefore, the larger REs segregate toward the outer surface of the crystal (Pianassola, Loveday, Chakoumakos *et al.*, 2020; Fukuda & Chani, 2007).

A microscope image and the EPMA results of sample J $(Dy_{1/2}Tb_{1/4}Gd_{1/4})_3Al_5O_{12}$ are shown in Fig. 6(b). The RE and Y concentration profiles are discontinuous, with a sharp increase in the center of the crystal. Closer to the outer surface of the crystal (from -1.5 to 0.6 mm and 0.5 to 1.4 mm), the profiles are located in the vicinity of the nominal concentration (7.5 at% for Dy and 3.75 at% for Tb and Gd). On the other hand, in the center of the crystal, all RE and Y have concentrations that are higher than the nominal, suggesting that the opaque and transparent regions are different phases.

The ratio between the sum of the concentrations of REs and Al obtained via EPMA can be used to confirm the phases that are present in the clear and opaque regions of the crystals. If we consider stoichiometric multicomponent aluminates, the nominal ratio should be 0.6 for garnet (RE₃Al₅O₁₂) and 1.0 for perovskite (REAlO₃). The experimental ratio was calculated for each EPMA data point shown in Fig. 6 to explain the discontinuity in elemental profiles. The average of this ratio for crystal A is 0.62 ± 0.003 , indicating a garnet phase for all data points. On the outer surface of crystal J (from -1.5 to 0.6 mm and 0.5 to 1.4 mm; Fig. 6), the average of this ratio is 0.6 ± 0.05 , indicating a garnet phase. In the center of crystal J, the average of this ratio is 1.0 ± 0.04 , indicating a perovskite phase; therefore, the central opaque region is caused by perovskite inclusions, which confirms the results from singlecrystal XRD.

5.5 A - (Lu_{1/4}Y_{1/4}Tb_{1/4}Gd_{1/4})₃Al₅O₁₂

5.0 Lu Y
Tb Gd

4.0
3.5
3.0
-1.5 -1.0 -0.5 0.0 0.5 1.0 1.5

Radial distance from crystal center (mm)

The formation of the perovskite phase only in the center of crystal J may be due to a higher melt temperature in the center of the molten zone (Samanta *et al.*, 2011) and may result in Al₂O₃ inclusions. At high temperatures, melts with a nominal garnet stoichiometry preferentially crystallize into a relatively simple orthorhombic perovskite structure rather than the more complex garnet structure (Bondar & Mezentseva, 1988).

A smaller amount of Al is consumed to form the perovskite (REAlO₃) phase than the garnet (RE₃Al₅O₁₂) phase and, therefore, after formation of the perovskite phase in the center, excess Al3+ remaining in the molten zone is accumulated near the periphery. According to our observations using a CCD camera, the growth interface was convex toward the melt. The shape of the interface leads to a radial crystal growth and segregation of excess Al3+ toward the outer surface of the crystal, inducing the formation of Al₂O₃ inclusions, as observed previously in Tb₃Al₅O₁₂ crystals (Ganschow et al., 2001). Alumina inclusions are discussed in §3.4. The convex shape of the solid-liquid interface may have been favored by the high crystallization temperature of the perovskite structure in the center of the crystal compared to the garnet structure near the outer surface. This difference in crystallization temperature is typical of the single-RE RE₂O₃-Al₂O₃ systems formed by the REs in composition J, namely Dy, Tb, and Gd (Wu & Pelton, 1992).

3.4. Inclusions on the outer surface of crystals

To investigate the morphology and composition of the inclusions seen on the outer surface of the crystals (Fig. 2), SEM images and EDS data were acquired from 1 mm-thick cross-sectional samples. Figs. 7(a) and 7(b) are SEM images of crystals C and J pulled fast, respectively; dark veins are close to the outer surface of the crystals and crystal J has a higher concentration of them. Similar dark inclusions are in crystals G–J pulled slowly and C–J pulled fast, and their concentration increases with increasing AIR (from C to J). Higher magnification images of crystals C and J shown in Figs. 7(c) and 7(d),

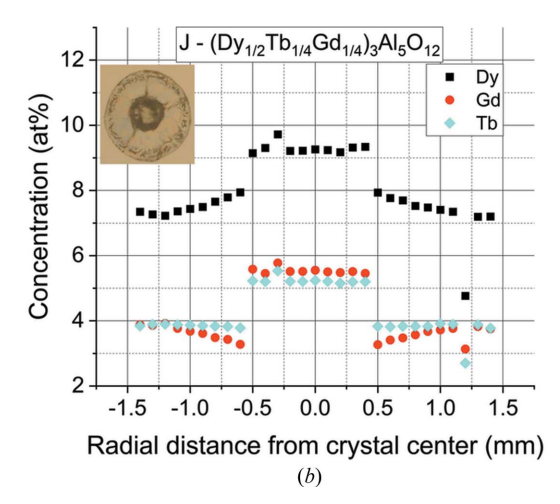


Figure 6
EPMA radial concentration profiles of crystals (a) A and (b) J grown from raw powders and pulled slowly. Measurements were done on 1 mm-thick radial sections cut 2 mm away from the seed end. In composition A, the nominal concentration is 3.75 at% for all REs. In composition J, the nominal concentration is 7.5 at% for Dy and 3.75 at% for Tb and Gd.

respectively, reveal that these dark veins are composed of entangled and interpenetrating lighter and darker phases, which is typical of a eutectic microstructure (Orera & Llorca, 2005). Alumina and eutectic inclusions near the outer surface of the crystals have been reported previously for mPD-grown single-RE garnets and have been attributed to incongruent melting in La:Lu₃Al₅O₁₂ (Bartosiewicz *et al.*, 2020) and a convex solid–liquid growth interface in Tb₃Al₅O₁₂ (Ganschow *et al.*, 2001).

To assess the elemental composition of the inclusions, EDS data were collected from the six points indicated in Fig. 7(d) and are presented in Table 3. Darker areas in the inclusions (points 1 and 2) have lower

concentrations of REs (Dy, Tb, and Gd) and are richer in Al, which indicates a secondary alumina phase that was below the detection limits of XRD techniques. Lighter areas in the inclusions (points 3 and 4) have relatively higher concentrations of REs than the dark areas, but still significantly lower than the nominal concentration; lighter areas are also rich in Al. On the other hand, outside of the inclusion (points 5 and 6), the concentration of REs and Al, and the measured stoichiometry, are closer to nominal.

The formation of eutectic inclusions may be related to composition. A larger AIR may induce the formation of eutectic inclusions since their concentration increases in compositions C to J. In the phase diagrams of single-RE RE₂O₃-Al₂O₃ systems, the position of the eutectic point between the single-RE garnet RE₃Al₅O₁₂ and Al₂O₃ is closer to the garnet stoichiometry as the RE ionic radius increases (Wu & Pelton, 1992; Bondar *et al.*, 1984). Therefore, the probability of forming eutectic inclusions during directional solidification increases for compositions with larger AIR and for regions in the crystal where larger elements are concentrated, such as the outer surface [Fig. 6(a)]. Additionally, the

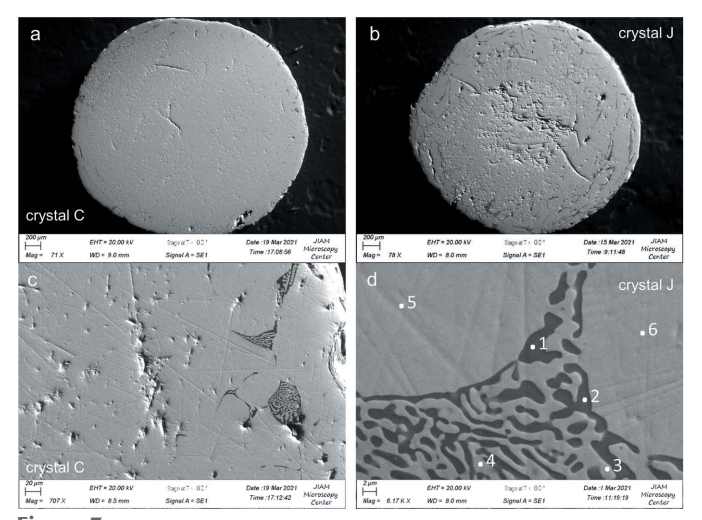


Figure 7 SEM images of crystals (a)/(c) C and (b)/(d) J grown from raw powders and pulled fast $(0.20 \text{ mm min}^{-1})$. EDS data obtained for points 1–6 in part (d) are given in Table 3.

Table 3 EDS elemental composition of crystal J grown fast for areas 1–6 shown in the SEM image in Fig. 7(d).

		EDS	elemen err					
Area	Points from Fig. $7(d)$	Dy	Tb	Gd	Al	О	Stoichiometry	
Nominal composition		7.5	3.75	3.75	25.00	60.00	$RE_3Al_5O_{12}$	
Darker area in the inclusion	1	1.63	0.87	0.91	46.06	50.53	$RE_{0.7}Al_{9.2}O_{10.1}$	
	2	1.60	0.87	0.93	46.27	50.33	RE _{0.7} Al _{9.3} O _{10.1}	
Lighter area in the inclusion	3	5.42	3.15	3.44	36.24	51.75	RE _{2.4} Al _{7.2} O _{10.4}	
-	4	4.54	2.79	3.30	37.80	51.57	$RE_{2.1}Al_{7.6}O_{10.3}$	
Outside the inclusion	5	7.70	3.90	3.80	31.60	53.00	$RE_{3.1}Al_{6.3}O_{10.6}$	
	6	7.35	3.99	4.16	32.37	52.13	$RE_{3.1}Al_{6.5}O_{10.4}$	

crystallization of a perovskite phase in the center of the crystal (discussed in §3.2 and §3.3) results in the rejection of Al^{3+} since the relative amount of Al in perovskites (REAlO₃) is lower than in garnets (RE₃Al₅O₁₂). This would lead to a molten zone rich in Al, which can shift the melt stoichiometry toward the eutectic composition.

4. Conclusion

We established a relation between the AIR of Y and RE elements and phase formation in multicomponent aluminum garnet crystals by growing and evaluating the phase composition of micro-pulling-down crystals of the system (Lu,Y,Ho,Dy,Tb,Gd)₃Al₅O₁₂. To determine this relation, ten compositions were formulated to obtain compounds within a relatively large range of AIR. In general, compositions with small AIR and slow pulling rates favor the formation of a single garnet phase. A central opaque region is formed in crystals with large AIR and has been attributed to a secondary perovskite phase. Additionally, a larger concentration of eutectic inclusions is formed at the outer surface of crystals with larger AIR.

Most crystals melted congruently and formed a single phase, even though 50% of the garnet dodecahedral sites were occupied by Tb³+ and Gd³+ (25% each), which form incongruent melting single-RE aluminum garnets. Although relatively large quantities of large Tb and Gd do not result in incongruent melting, large AIR induces the formation of secondary perovskite and eutectic phases. Future exploration of the fundamental and functional properties of multicomponent garnet crystals could include compositions with Tb and Gd in relatively large concentrations without inducing secondary phases, as long as the AIR is maintained lower than 1.038 Å, which here corresponds to the composition I.

Acknowledgements

This project was supported by the National Science Foundation. One of the authors is grateful for the support from the Center for Materials Processing, University of Tennessee. Electron microprobe measurements were performed at the

Electron Microprobe Laboratory in the Department of Earth and Planetary Sciences at the University of Tennessee, Knoxville, with the assistance of Molly McCanta and Allan Patchen. X-ray diffraction experiments were performed at the Institute for Advanced Materials & Manufacturing (IAMM) Diffraction Facility located at the University of Tennessee, Knoxville. A portion of this research used resources at the Spallation Neutron Source, a DOE Office of Science User Facility operated by the Oak Ridge National Laboratory.

Funding information

Funding for this research was provided by: National Science Foundation (grant No. DMR 1846935).

References

- Bartosiewicz, K., Horiai, T., Yamaji, A., Yoshikawa, A., Kurosawa, S., Yoshino, M. & Zorenko, Y. (2020). *Mater. Sci. Eng. B*, **261**, 114677.
- Bombik, A., Leśniewska, B., Mayer, J. & Pacyna, A. W. (2003). *J. Magn. Magn. Mater.* **257**, 206–219.
- Bondar, I. A., Koroleva, L. N. & Bezruk, E. T. (1984). *Izv. Akad. Nauk SSSR Neorg. Mater.* **20**, 257–261.
- Bondar, I. A. & Mezentseva, L. P. (1988). Progr. Cryst. Growth Charact. 16, 81–141.
- Braun, J. L., Rost, C. M., Lim, M., Giri, A., Olson, D. H., Kotsonis,
 G. N., Stan, G., Brenner, D. W., Maria, J.-P. & Hopkins, P. E. (2018).
 Adv. Mater. 30, 1805004.
- Chen, H., Zhao, Z., Xiang, H., Dai, F. Z., Xu, W., Sun, K., Liu, J. & Zhou, Y. (2020). J. Mater. Sci. Technol. 48, 57–62.
- Chen, Y. W., Ruan, J. J., Ting, J. M., Su, Y. H. & Chang, K. S. (2021). Ceram. Int. 47, 11451–11458.
- Chewpraditkul, W., Pattanaboonmee, N., Sakthong, O., Chewpraditkul, W., Szczesniak, T., Moszynski, M., Kamada, K., Yoshikawa, A. & Nikl, M. (2018). *Opt. Mater.* **76**, 162–168.
- Djenadic, R., Sarkar, A., Clemens, O., Loho, C., Botros, M., Chakravadhanula, V. S. K., Kübel, C., Bhattacharya, S. S., Gandhi, A. S. & Hahn, H. (2017). *Mater. Res. Lett.* **5**, 102–109.
- Farrugia, L. J. (2012). J. Appl. Cryst. 45, 849-854.
- Fukuda, T. & Chani, V. I. (2007). In Shaped Crystals: Growth by the Micro-Pulling-Down Technique. Berlin, Heidelberg: Springer.
- Ganschow, S., Klimm, D., Epelbaum, B. M., Yoshikawa, A., Doerschel, J. & Fukuda, T. (2001). J. Cryst. Growth, 225, 454–457.
- Greculeasa, M., Broasca, A., Voicu, F., Hau, S., Croitoru, G., Stanciu, G., Gheorghe, C., Pavel, N. & Gheorghe, L. (2020). Opt. Laser Technol. 131, 106433.
- Hammann, J. (1969). Acta Cryst. B25, 1853-1856.
- Jacobson, V., Diercks, D., To, B., Zakutayev, A. & Brennecka, G. (2021). J. Eur. Ceram. Soc. 41, 2617–2624.
- Kamada, K., Prusa, P., Nikl, M., Blazek, K., Endo, T., Tsutsumi, K., Kurosawa, S., Yokota, Y. & Yoshikawa, A. (2014). *IEEE Trans. Nucl. Sci.* **61**, 293–296.
- Kamada, K., Yanagida, T., Pejchal, J., Nikl, M., Endo, T., Tsutumi, K., Fujimoto, Y., Fukabori, A. & Yoshikawa, A. (2011). *J. Phys. D Appl. Phys.* 44, 505104–505112.
- Karati, A., Parida, T., Gupta, J., Adigilli, H. K., Borse, P. H. & Joardar, J. (2021). Mater. Res. Bull. 137, 111181.

- Kinsler-Fedon, C., Zheng, Q., Huang, Q., Choi, E. S., Yan, J., Zhou, H., Mandrus, D. & Keppens, V. (2020). *Phys. Rev. Mater.* 4, 104411.
- Kirnbauer, A., Spadt, C., Koller, C. M., Kolozsvári, S. & Mayrhofer, P. H. (2019). *Vacuum*, **168**, 108850.
- Kotsonis, G. N., Meisenheimer, P. B., Miao, L., Roth, J., Wang, B., Shafer, P., Engel-Herbert, R., Alem, N., Heron, J. T., Rost, C. M. & Maria, J. P. (2020). Phys. Rev. Mater. 4, 100401.
- Kotsonis, G. N., Rost, C. M., Harris, D. T. & Maria, J. P. (2018). MRS Commun. 8, 1371–1377.
- Li, J. G. & Sakka, Y. (2015). Sci. Technol. Adv. Mater. 16, 014902.
- Liang, Y., Luo, B., Dong, H. & Wang, D. (2021). Ceram. Int. 47, 20196– 20200.
- Liu, F., Dong, L., Cao, S., Chen, J., Xu, H., Han, W. & Liu, J. (2021). J. Cryst. Growth, 558, 126023.
- Meisenheimer, P. B., Kratofil, T. J. & Heron, J. T. (2017). Sci. Rep. 7, 1–6.
- Musicó, B. L., Gilbert, D., Ward, T. Z., Page, K., George, E., Yan, J., Mandrus, D. & Keppens, V. (2020). APL Mater. 8, 040912.
- Nguyen, M. H., Lee, S. J. & Kriven, W. M. (1999). J. Mater. Res. 14, 3417–3426.
- Nguyen, T. X., Su, Y. H., Hattrick-Simpers, J., Joress, H., Nagata, T., Chang, K. S., Sarker, S., Mehta, A. & Ting, J. M. (2020). *ACS Comb. Sci.* **22**, 858–866.
- Orera, V. M. & Llorca, J. (2005). Encyclopedia of *Mater. Sci. Technol.* pp. 1–9 Amsterdam: Elsevier.
- Patel, R. K., Ojha, S. K., Kumar, S., Saha, A., Mandal, P., Freeland, J. W. & Middey, S. (2020). Appl. Phys. Lett. 116, 071601.
- Pianassola, M., Loveday, M., Chakoumakos, B. C., Koschan, M., Melcher, C. L. & Zhuravleva, M. (2020). Cryst. Growth Des. 20, 6769–6776.
- Pianassola, M., Loveday, M., McMurray, J. W., Koschan, M., Melcher, C. L. & Zhuravleva, M. (2020). J. Am. Ceram. Soc. 103, 2908–2918.
- Pianassola, M., Stand, L., Loveday, M., Chakoumakos, B. C., Koschan, M., Melcher, C. L. & Zhuravleva, M. (2021). Phys. Rev. Mater. 5, 083401.
- Prusa, P., Kamada, K., Nikl, M., Yoshikawa, A. & Mares, J. A. (2013). *Radiat. Meas.* **56**, 62–65.
- Rigaku OD (2015). CrysAlis PRO. Rigaku Oxford Diffraction Ltd, Yarnton, Oxfordshire, England.
- Rost, C. M., Sachet, E., Borman, T., Moballegh, A., Dickey, E. C., Hou, D., Jones, J. L., Curtarolo, S. & Maria, J. P. (2015). *Nat. Commun.* **6**, 1–8.
- Samanta, G., Yeckel, A., Daggolu, P., Fang, H., Bourret-Courchesne, E. D. & Derby, J. J. (2011). J. Cryst. Growth, 335, 148–159.
- Shannon, R. D. & Prewitt, C. T. (1969). Acta Cryst. B25, 925-946.
- Sharma, Y., Mazza, A. R., Musico, B. L., Skoropata, E., Nepal, R., Jin, R., Ievlev, A. V., Collins, L., Gai, Z., Chen, A., Brahlek, M., Keppens, V. & Ward, T. Z. (2021). Appl. Mater. Interfaces, 13, 17971–17977.
- Sharma, Y., Musico, B. L., Gao, X., Hua, C., May, A. F., Herklotz, A., Rastogi, A., Mandrus, D., Yan, J., Lee, H. N., Chisholm, M. F., Keppens, V. & Ward, T. Z. (2018). *Phys. Rev. Mater.* **2**, 060404.
- Sheldrick, G. M. (2015). Acta Cryst. C71, 3-8.
- Sivakumar, S., Zwier, E., Meisenheimer, P. B. & Heron, J. T. (2018). *J. Vis. Exp.* **2018**, e57746.
- Sun, L., Luo, Y., Ren, X., Gao, Z., Du, T., Wu, Z. & Wang, J. (2020).
 Mater. Res. Lett. 8, 424–430.
- Wu, P. & Pelton, A. D. (1992). J. Alloys Compd. 179, 259–287.